

Spectral Engineering of Cavity-Protected Polaritons in an Atomic Ensemble with Controlled Disorder

Mohamed Baghdad,^{1,*} Pierre-Antoine Bourdel,^{1,*} Sylvain Schwartz,^{1,2,*} Francesco Ferri,¹ Jakob Reichel,¹ and Romain Long^{1,†}

¹*Laboratoire Kastler Brossel, ENS-Université PSL, CNRS, Sorbonne Université, Collège de France, 24 rue Lhomond, Paris, 75005, France*

²*Present address: DPHY, ONERA, Université Paris-Saclay, 91123 Palaiseau, France.*

(Dated: August 26, 2022)

The paradigm of N quantum emitters coupled to a single cavity mode appears in many situations ranging from quantum technologies to polaritonic chemistry. The ideal case of identical emitters is elegantly modeled in terms of symmetric states, and understood in terms of polaritons. In the practically relevant case of an inhomogeneous frequency distribution, this simple picture breaks down and new and surprising features appear. Here we leverage the high degree of control in a strongly coupled cold atom system, where for the first time the ratio between coupling strength and frequency inhomogeneities can be tuned. We directly observe the transition from a disordered regime to a polaritonic one with only two resonances. The latter are much narrower than the frequency distribution, as predicted in the context of “cavity protection”. We find that the concentration of the photonic weight of the coupled light-matter states is a key parameter for this transition, and demonstrate that a simple parameter based on statistics of transmission count spectra provides a robust experimental proxy for this theoretical quantity. Moreover, we realize a dynamically modulated Tavis-Cummings model to produce a comb of narrow polariton resonances protected from the disorder, with potential applications to quantum networks.

While the foundations of cavity quantum electrodynamics (CQED) have been laid with single-emitter systems [1, 2], the extension to many emitters coupled to the same cavity mode holds interest for many different communities [3–6]. In solid-state systems, with emitters such as rare earth ions, color centers in diamond, or semiconductor quantum wells, the N -emitter situation arises naturally and is exploited to enhance the light-matter coupling beneficial for quantum network implementations [7–9]. In atomic systems, the coupling between emitters via the cavity mode is a powerful approach for generating different forms of many-particle entanglement [10–12] including spin-squeezed states for quantum metrology [13–17]. When combined with a high degree of control over the emitter qubits, this is the basis for an emerging form of quantum simulations of long-range coupled spin systems [5, 18–21]. All these experiments operate in the regime of low excitation, with no more than one photon present in the cavity, and are performed in the regime of strong collective coupling, or even strong single-emitter coupling.

Central to such systems is the notion of a polariton [22], the hybrid light-matter state composed of an intracavity photon and the ensemble of emitters sharing a single excitation. In homogeneous systems where all emitters have the same resonance frequency ω_0 , the energy spectrum of the coupled system is the well-known avoided crossing with only two resonances. Although many more, less symmetric atomic states exist, they do not participate in the system’s transmission or reflection spectra because they are “dark”: their collective coupling to the photonic mode vanishes. However, as soon as there

is frequency inhomogeneity in the emitter ensemble, this destructive interference is no longer complete, and the formerly dark states now couple to the light field, becoming “gray”. While frequency inhomogeneity is easily included in the foundational Tavis-Cummings Hamiltonian [23], it leads to rich and often surprising physics, as shown by many recent advances driven by the interplay of theory and experiment. One spectacular example in the field of materials science started with the discovery that coupling an organic semiconductor to a cavity can profoundly change its material properties, and in particular, enhance its conductivity through the hybridization of electronic transitions [24]. Recent theoretical advances point out the importance of the “gray” states in the localization and transport properties of these systems [25–28].

In this context, atomic CQED systems with their high degree of control appear as a promising tool for quantum simulation [29] of such CQED-enhanced materials. Another prominent example is the phenomenon of “cavity protection”: a system with strong inhomogeneous broadening can still support narrow resonances (much narrower than the width of the broadening) under certain conditions [30–32]. Cavity protection has been experimentally demonstrated recently in the context of solid-state CQED [9, 33, 34], where inhomogeneous broadening is dictated by material properties and the narrow resonances warrant hope for quantum memories with long coherence times despite fast dephasing of the uncoupled emitters. Clearly, the features of such a system depend on the relative strength of the broadening. However, this is usually not adjustable in solid-state systems, precluding a direct observation of the transition to the protected

regime, from which a better understanding of the physics would emerge.

In this article, we present results of an atomic CQED experiment with tunable atomic frequency distribution. We experimentally show the transition from a “protected” regime where only two polaritonic resonances are present despite an inhomogeneous frequency distribution that is much larger than the polariton resonances, to an “unprotected” one where the amplitude of the polaritons decreases and many additional, randomly distributed resonances appear. Our analysis shows that the number of photon counts outside the two narrow polariton peaks acts as a robust experimental proxy that closely traces the calculated photonic weight of the gray states. In addition, as our system operates in the strong coupling regime at the single atom level, we are able to study this transition for a few tens of atoms, several orders of magnitude lower than previous experiments, highlighting the contribution of a finite number of dark states. Finally, we produce polaritons featuring a comb-like frequency spectrum by modulating the light-shifted frequency of the atoms on a very fast time scale in the protected regime. This allows us to shape the frequency spectrum of the system, with possible applications to quantum memories and quantum communications [35–38].

COLD ATOM CAVITY INTERFACE WITH TUNABLE FREQUENCY INHOMOGENEITY

In our experiment, a cold ensemble of Rubidium atoms is trapped inside a high-finesse Fabry-Perot microcavity [39] with a length of $140\ \mu\text{m}$. The number of atoms loaded into the cavity can be varied between a few tens and a few thousands (see Methods). Unless otherwise noted, atoms are initially prepared in $|g\rangle = |5S_{1/2}, F=2, m_F=2\rangle$. The probe beam exciting the cavity mode on the D2 line of ^{87}Rb at $780\ \text{nm}$ is circularly polarized, coupling $|g\rangle$ to the excited state $|e\rangle = |5P_{3/2}, F'=3, m_{F'}=3\rangle$. The choice of circular polarization is possible thanks to the negligible birefringence of our cavity [40]. To realize a homogeneous and maximal coupling of all the atoms, they are trapped at the antinodes of the cavity mode. This is achieved by an intracavity standing wave at $\omega_t = 2\pi c_0/1559\ \text{nm}$ where c_0 is the speed of light, which is commensurate with the atomic line taking into account the Gouy phase shift and the phase shift at reflection on the mirrors [41, 42]. The dipole light is linearly polarized and the trap depth of the intracavity lattice can be adjusted between $300\ \mu\text{K}$ and $1400\ \mu\text{K}$ with atomic temperatures ranging from $50\ \mu\text{K}$ to $160\ \mu\text{K}$. The maximum single-atom coupling is $g_0/2\pi \simeq 76\ \text{MHz}$; thermal motion leads to a temperature-dependent average single-atom coupling $g/2\pi$ between 55 and 68 MHz (see Supplementary Information). This is larger than the cavity decay rate

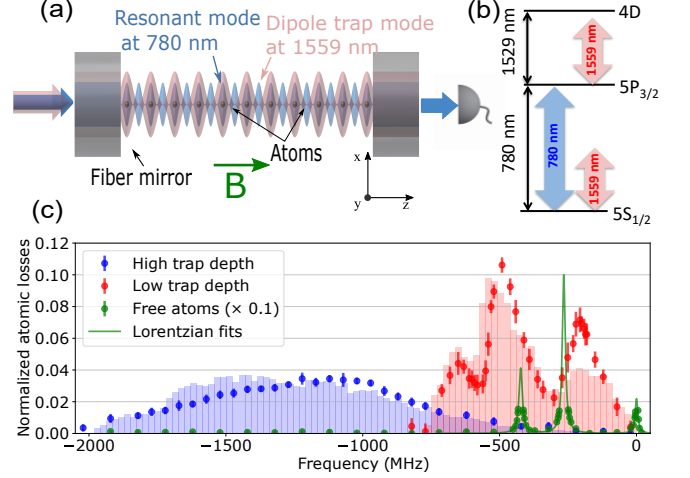


FIG. 1. Experimental setup of the cold atom cavity interface with tunable inhomogeneous frequency distribution. (a) Sketch of the setup. Atoms are trapped in a one-dimensional optical lattice (red) which is commensurate with the main cavity mode (blue). The latter is on resonance with the $|g\rangle \leftrightarrow |e\rangle$ atomic transition. (b) Simplified level diagram illustrating the proximity of the $1559\ \text{nm}$ trapping light with the $5P_{3/2} \leftrightarrow 4D$ line. (c) Atomic frequency distribution measured by loss spectroscopy of the trapped atoms for various trap depths (Green: no trap. Red: $U = 310\ \mu\text{K}$. Blue: $U = 1400\ \mu\text{K}$). The horizontal axis corresponds to the frequency of the transverse probe beam inducing the losses, referenced to the bare $|5S_{1/2}, F=2, m_F=2\rangle \leftrightarrow |5P_{3/2}, F'=3, m_{F'}=3\rangle$ transition. Circles: experimentally measured losses (error bars correspond to 1σ spread of the data), normalized to the maximum value of the $F'=2$ peak of the free atoms. Histograms: result of Monte Carlo simulations of the frequency distributions (see main text and Supplementary Information).

(HWHM) $\kappa/2\pi \simeq 15\ \text{MHz}$ and the spontaneous emission rate $\gamma/2\pi \simeq 3\ \text{MHz}$, placing the system in the strong coupling regime of CQED.

Due to a nearby resonance (the $5P_{3/2} \leftrightarrow 4D$ transition at $1529\ \text{nm}$), the trapping light induces a light shift of the excited state of the D2 line which is $\simeq 50$ times larger than the ground state light shift [43]. Thus, it creates an adjustable shift and broadening of the frequency distribution of the $|g\rangle \leftrightarrow |e\rangle$ transition, the latter depending also on the finite temperature of the trapped atoms (see Methods). We characterize the frequency distribution experimentally by illuminating the trapped atoms with a transverse beam and measuring the relative atomic losses as a function of the beam frequency for various trap depths, as shown on Fig. 1 (c). It shows the broadening (up to $1\ \text{GHz}$) and shift due to the $1559\ \text{nm}$ light power. A Monte Carlo simulation assuming an initial atomic population uniformly distributed between all the Zeeman sublevels, but no subsequent redistribution or depumping (see Methods), is in qualitative agreement with the experimental loss curves.

CAVITY PROTECTION EFFECT

To investigate the coherence properties of this inhomogeneous system, we consider the transmission spectrum of the cavity in the low excitation limit, which is relevant for our experimental configuration. We start by describing the homogeneous case. For a cavity mode resonant with the atomic line in the strong coupling regime, the spectrum exhibits the well-known vacuum Rabi splitting featuring two peaks $2g\sqrt{N}$ apart in frequency, where N is the atom number, and their width is given by $(\kappa + \gamma)/2$ [2]. They correspond to two polaritons of the form:

$$|P_{\pm}\rangle = \frac{1}{\sqrt{2}} (|1, G\rangle \pm |0, W\rangle), \quad (1)$$

where $|1, G\rangle$ is the state with one photon in the cavity mode and all atoms in the ground state and $|0, W\rangle$ is a state with zero photons in the cavity mode and one excitation symmetrically shared between the atoms. In addition, $N - 1$ degenerate dark states are not coupled to the cavity light field. This is reflected in the photonic weight (PW), which is defined by the overlap of the eigenstates of the coupled system $|\psi_{\alpha}\rangle$ with $|1, G\rangle$, $PW = |\langle G, 1|\psi_{\alpha}\rangle|^2$ [44], and is zero for all eigenstates except $|P_{\pm}\rangle$.

In our experiment, two types of inhomogeneities are present. First, each atom k has a different value of the coupling g_k to the cavity. This does not change the previous result, except that the splitting is now given by 2Ω , where $\Omega = \sqrt{\sum_{k=1}^N g_k^2}$ is the collective coupling and $|W\rangle = \Sigma^{\dagger} |G\rangle$ with $\Sigma^{\dagger} = \sum_{k=1}^N \frac{g_k}{\Omega} \sigma_k^{\dagger}$, σ_k^{\dagger} being the raising operator for atom k . Secondly, each atom has a different light-shifted atomic frequency ω_k depending on its motional state in the trapping potential and this leads to more profound modifications. In the strong coupling limit, two hybrid light-matter collective modes (denoted simply polaritons in the following) still exist and are split by $\simeq 2\Omega$. However, their coherence is limited as they are coupled to the $N - 1$ other eigenstates, that we denote *dark states* in the following as they carry zero photonic weight for infinite coupling. This coupling can be strongly reduced if there is an energy gap between the polaritons and the dark states. This is achieved when the energy gap, given by Ω , is much larger than the atomic frequency distribution width $\Delta\omega$ [30–32].

For our specific system, we compute the spectral distribution of the coupling of the atomic ensemble with the cavity field: $\rho(\omega) = \sum_{k=1}^N \sum_{j=1}^{16} g_{k,j}^2 \delta(\omega - \omega_{k,j})$, where we sum over all 16 excited sublevels of the $5P_{3/2}$ manifold (see Supplementary). The distribution is shown in Fig. 2 for a trap depth of $\approx 1400 \mu\text{K}$. It has an asymmetrical shape and features a bounded support 1700 MHz wide, which corresponds to the highest possible value of the light shift for this trap depth. The frequency ω_c of the cavity mode is tuned to resonance with the mean

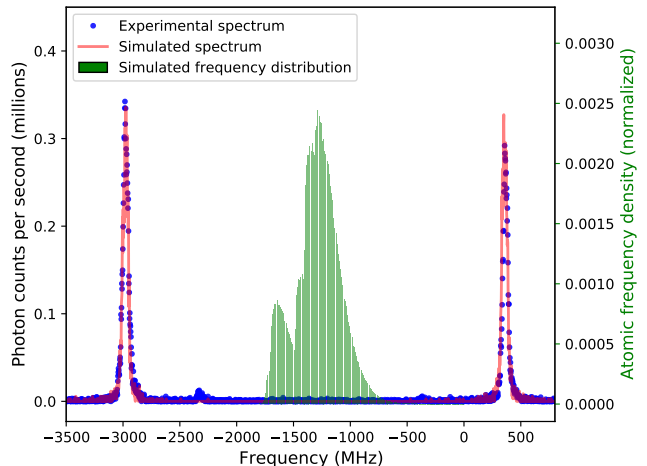


FIG. 2. **Cavity protection effect.** Blue dots represent the experimental on-resonance transmission spectrum in the regime where the collective coupling is much larger than the atomic frequency distribution. The two polariton modes appear as two narrow transmission peaks, in good agreement with the numerical simulation (red line). Green bars show the simulated atomic frequency distribution, which is much broader than the transmission peaks.

value of the frequency distribution. The experimental transmission spectrum of the cavity averaged over ≈ 200 spectra is also represented in Fig. 2. Despite the broad atomic frequency distribution, it features only two peaks corresponding to the polaritons. To first order in $\Delta\omega/\Omega$ with $\Delta\omega$ the width of the frequency distribution, they are split by twice the collective coupling $\Omega/2\pi \simeq 1670 \text{ MHz}$, which corresponds to $N \approx 770$ atoms trapped in the cavity mode. In this regime, we fully benefit from the “cavity protection” effect: the two polaritons lying outside the distribution support, they are decoupled from the dark states and the coherence of the system is preserved.

The fitted width of the peak $\delta\omega/2\pi = 26 \pm 2 \text{ MHz}$ is much lower than the width $\Delta\omega/2\pi \approx 150 \pm 10 \text{ MHz}$ of the frequency distribution (see Methods). The ratio $\frac{\Delta\omega/2}{\delta\omega}$ can be used to define a figure of merit of the cavity protection. It allows the comparison between the measured width $\delta\omega$ of the polaritonic peaks and the width $\Delta\omega/2$ that would be obtained for a Lorentzian probability distribution inhibiting the protection effect [30–32]. This ratio is about 3 for our experiment, showing that despite strong inhomogeneities, the coherence of the polaritons can be preserved as long as $\Omega \gg \Delta\omega$ for our frequency distribution. We note that the measured widths are larger than the homogeneous limit of $(\kappa + \gamma)/2 \simeq 9 \text{ MHz}$, mainly due to shot-to-shot fluctuations of the atom number, which broadens the averaged peaks by inducing a jittering of the collective coupling. The widths are indeed the same for the different trap depths used in the experiment within the error margins.

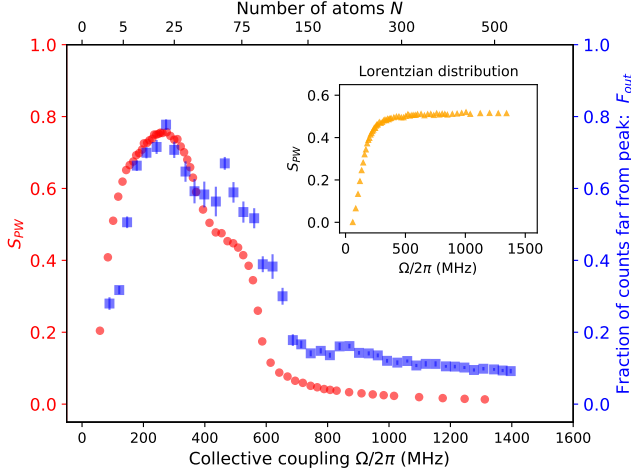


FIG. 3. **Transition from the unprotected to the protected regime.** For a given atomic frequency distribution, we increase the number of atoms and thus the collective coupling. Blue squares: measured F_{out} . Beyond a collective coupling $\Omega_{th}/(2\pi) \simeq 300$ MHz, the fraction of photon counts outside the two polariton peaks rapidly drops. F_{out} is closely traced by the simulated photonic weight S_{PW} (red circles): confirming that the off-peak transmission corresponds to gray states whose photonic weight drops as faster coupling wins over disorder-induced dephasing. For comparison, the inset shows S_{PW} in the case of a Lorentzian resonance frequency distribution. Since no cavity protection occurs in this case, S_{PW} remains high at large collective coupling.

As can be seen on Fig.2, the simulated spectra including atom number fluctuations are in excellent agreement with the experimental data.

TRANSITION FROM THE UNPROTECTED TO THE PROTECTED REGIME

Exploiting the high degree of control of our system, we explore the transition from the unprotected to the protected regime. To exhibit this transition, we acquire cavity transmission spectra as a function of the number N of trapped atoms in the cavity mode, for $10 \lesssim N \lesssim 550$. As we are dealing with a mesoscopic number of atoms, we can compute the photonic weight of the different eigenstates of the coupled system for the trap depth and atom temperature of the experiment. The cavity protection effect can directly be assessed by measuring the distribution of the PW s over the different eigenstates. For a system with inhomogeneity of the emitter frequencies, the PW is distributed over more than two eigenstates. This leads us to introduce the sum S_{PW} of the PW of all the eigenstates except the two largest ones, to quantify the spreading of the PW and thus the coherence of the coupled system: S_{PW} is zero for the homogeneous case and tends to 1 when the PW is distributed over an

infinite number of dark states.

Experimentally, as we stay in the low-excitation limit, the small number of collected photons per spectrum prevents the direct measurement of the PW of the eigenstates. Instead, we extract from each spectrum the fraction F_{out} of photon counts that are outside of two narrow frequency windows corresponding to the polariton peaks (see Methods). The width Δf of these windows is chosen such that they contain about 90% of the counts in the protected regime.

The results are shown in Fig.3. Starting from zero atoms, F_{out} increases with N , reaches a maximum for a measured coupling $\Omega/(2\pi) \simeq 300$ MHz corresponding to $N \simeq 25$ atoms, and then decreases to an asymptotic value. As expected, we find that the shape of F_{out} data is robust against the choice Δf (see Fig. E3) and closely traces the calculated S_{PW} (see Methods). This allows us to interpret the common behavior of F_{out} and S_{PW} in terms of two competing effects. As N increases, the dimension $(N+1)$ of the Hilbert space of the system rises, and so does the number of states available to carry part of the photonic excitation outside Δf . The collective coupling Ω also increases (scaling as \sqrt{N}), and spreads the PW s to eigenstates close in frequency of Ω as long as the system stays in the unprotected regime $\Omega \ll \Delta\omega$. Then, above a certain value of the collective coupling Ω_{th} , the cavity protection effect starts to reduce S_{PW} and F_{out} . In the large collective coupling limit, S_{PW} and F_{out} are low, because the photonic weight - and thus the photon counts - concentrate in the two polaritonic states. To underscore the role of cavity protection contribution, we simulate S_{PW} for a Lorentzian distribution with the same average frequency and width as the experimental one. In this case (see in Fig. 3), after the initial increase, S_{PW} stays on a plateau as no cavity protection occurs. For our system, we note that the protection effect starts to play a role for a mesoscopic number of a few tens of atoms, which is several orders of magnitude lower than the typical number of emitters involved in solid-state based systems [9, 33]. This allows us to explore this effect for a finite-sized system, and to directly observe the PW concentration in the two polaritons.

SPECTRAL ENGINEERING OF POLARITONS

The coherence of the polaritons being preserved by the cavity protection, we can then harness the large sensitivity of the light-shifted atomic frequency to the trapping power to efficiently modulate the polaritonic frequencies. The intracavity dipole power is modulated by coupling two different frequencies of the dipole light into the cavity. The resulting beating at a frequency $\omega_m/2\pi$ leads to a modulation of the dipole potential and thus of the average light-shifted frequency of the atoms $\bar{\omega}_A(t) = \bar{\omega}_A^0 + \beta_o \omega_m \cos(\omega_m t)$ where β_o is the modulation

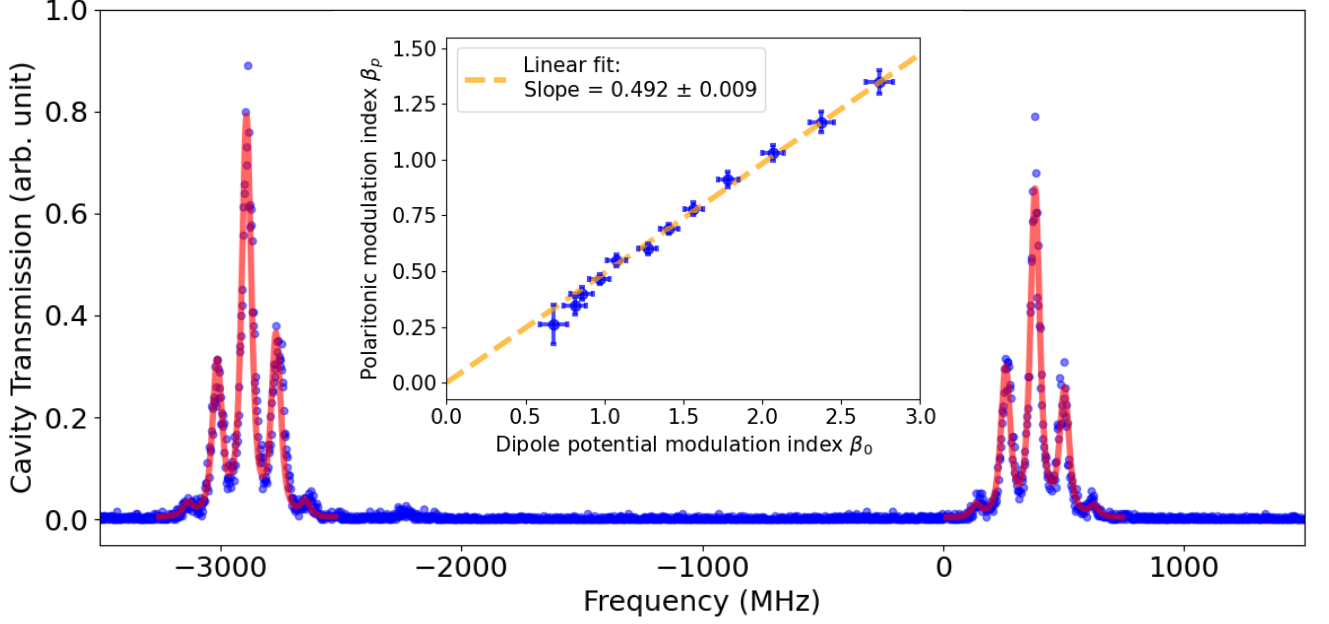


FIG. 4. **Modulation of the polariton eigenfrequencies.** Blue points: experimental data with $\Omega/2\pi = 1630 \pm 20$ MHz, $\omega_m/2\pi = 120$ MHz, $\beta_o = 2.17 \pm 0.04$. Red line: simulated spectrum obtained by numerically integrating the master equation. Inset: Modulation transfer function. Blue points: experimental data of the modulation index of the polaritons β_p for different values of the modulation index β_o of the atomic frequency. Red dashed line: linear fit of data points gives a slope of 0.492 ± 0.009 , compatible with the theoretical slope of 0.5.

index and $\bar{\omega}_A^0$ the average atomic frequency without modulation. The modulation frequency $\omega_m/2\pi \sim 125$ MHz is set to be larger than the width of the polaritons but smaller than the collective coupling Ω . We record the transmission spectrum following the same procedure as before and average about 200 spectra. The results are presented in Fig. 4. Instead of the usual polariton doublet, the spectrum features two combs each consisting of several peaks. The frequency splitting between the centers of the two combs is given by the collective coupling $\Omega/2\pi$ whereas the comb teeth are separated by the modulation frequency $\omega_m/2\pi$. In contrast to the experiment of Ref. [45] where $\omega_m \gg \Omega$, the transmission spectrum does not result from the coupling between the cavity field and a single-frequency atomic excitation given by one sideband of the modulated atomic transition. In our case, the photonic excitation couples to a multi-frequency atomic excitation, yielding polaritons featuring multiple frequencies in their spectrum.

For $\omega_m \ll \Omega$, the theoretical cavity spectrum is well approximated by (see Supplementary Information)

$$S(\omega) \propto \sum_n \frac{J_n^2(\beta_o/2)}{(\omega - \omega_0 - n\omega_m + \Omega)^2 + \gamma_s^2} + \frac{J_n^2(\beta_o/2)}{(\omega - \omega_0 - n\omega_m - \Omega)^2 + \gamma_s^2} \quad (2)$$

where $\omega_0 = \omega_c = \bar{\omega}_A^0$ and $\gamma_s = \frac{\kappa + \gamma}{2}$. Based on this ex-

pression, we define a modulation index for the polaritons given by $\beta_p = \beta_o/2$. We have measured β_p for different values of β_o (see inset of Fig. 4), and find very good agreement with the expected slope. The spectrum of the polaritons can thus be directly controlled by tuning the modulation index and/or the modulation frequency. This is possible thanks to the large sensitivity of the excited state to the trapping power. An important remark is that the width of each peak in the multi-frequency polaritons is similar to the ones obtained in the non-modulated case and is much narrower than the atomic frequency distribution as we operate in the cavity protected regime. A slight asymmetry between the right and left part of each comb is clearly visible on Fig. 4. This asymmetry, stemming from the coupling between the two polaritons induced by the modulation, is well reproduced in the simulated spectrum obtained by numerically integrating the master equation (see Methods and Supplementary Information).

Polaritons with multi-frequency components and yet small linewidth created using this new technique can lead to applications in quantum network for spectral shaping of single-photon emission [35, 36, 46]. More generally, the highly controlled experimental platform described here is ideally suited to study the role of inhomogeneities and disorder in strong light-matter interfaces. It has already allowed us to observe and quantitatively

describe the transition between the protected and the unprotected regimes, yielding a better understanding of the role of dark states. It can be extended to generate a new kind of entangled dark states through collective dissipation useful for quantum sensing and quantum simulation, as recently proposed [47], and to investigate the regime of higher excitation which has been little explored so far [48]. Moreover, when combined with addressing capabilities [21, 49–51], controllable disorder as demonstrated here will allow the study of transport in disordered ensembles, with the perspective to quantum simulate the properties of engineered polaritonic materials [28, 44].

Note: While preparing this manuscript, we became aware of related results in the group of J.-P. Brantut (EPFL Lausanne) [52], and both groups decided to coordinate their submissions.

Acknowledgments We thank G. Pupillo and J. Schachenmayer for discussion within the ANR project CLIMAQS. This project has received funding from: Agence Nationale de la Recherche (ANR) (SAROCMA project, ANR-14-CE32-0002); European Research Council (ERC) under the European Union’s Horizon 2020 research and innovation programme Grant agreement No 671133 (EQUEMI project). It has been supported by Region Ile-de-France in the framework of DIM SIRTEQ. S. Schwartz acknowledges funding from the European Union under the Marie Skłodowska Curie Individual Fellowship Programme H2020-MSCA-IF-2014 (project No. 658253)

Authors’ contributions M.B., F.F. and R.L. built the experimental setup, M.B., P.-A.B., S.S. and R.L. performed the measurements and analyzed the data. P.-A.B., S.S., F.F., J.R. and R.L. interpreted the results and wrote the manuscript with input from all authors.

Competing interests The authors declare no competing interests.

Data and materials availability The data that support the findings of this study are available from the corresponding authors upon reasonable request.

* These authors contributed equally to this work.

† long@lkb.ens.fr

- [1] H. J. Kimble, Strong interactions of single atoms and photons in cavity QED, *Phys. Scr.* **1998**, 127 (1998).
- [2] S. Haroche and J.-M. Raimond, *Exploring the Quantum: Atoms, Cavities, and Photons* (Oxford University Press, 2006).
- [3] D. D. Solnyshkov, G. Malpuech, P. St-Jean, S. Ravets, J. Bloch, and A. Amo, Microcavity polaritons for topological photonics [Invited], *Opt. Mater. Express* **11**, 1119 (2021).
- [4] A. Blais, S. M. Girvin, and W. D. Oliver, Quantum information processing and quantum optics with circuit quantum electrodynamics, *Nat. Phys.* **16**, 247 (2020).
- [5] D. E. Chang, J. S. Douglas, A. González-Tudela, C.-L.

- Hung, and H. J. Kimble, Colloquium: Quantum matter built from nanoscopic lattices of atoms and photons, *Rev. Mod. Phys.* **90**, 031002 (2018).
- [6] T. W. Ebbesen, Hybrid light-matter states in a molecular and material science perspective, *ACCOUNTS OF CHEMICAL RESEARCH* **49**, 2403 (2016).
- [7] F. Bussi eres, N. Sangouard, M. Afzelius, H. de Riedmatten, C. Simon, and W. Tittel, Prospective applications of optical quantum memories, *Journal of Modern Optics* **60**, 1519 (2013).
- [8] K. Heshami, D. G. England, P. C. Humphreys, P. J. Bustard, V. M. Acosta, J. Nunn, and B. J. Sussman, Quantum memories: Emerging applications and recent advances, *J Mod Opt* **63**, 2005 (2016).
- [9] T. Zhong, J. M. Kindem, J. Rochman, and A. Faraon, Interfacing broadband photonic qubits to on-chip cavity-protected rare-earth ensembles, *Nat Commun* **8**, 14107 (2017).
- [10] F. Haas, J. Volz, R. Gehr, J. Reichel, and J. Esteve, Entangled States of More Than 40 Atoms in an Optical Fiber Cavity, *Science* **344**, 180 (2014).
- [11] R. McConnell, H. Zhang, J. Hu, S.  uk, and V. Vuleti , Entanglement with negative Wigner function of almost 3,000 atoms heralded by one photon, *Nature* **519**, 439 (2015).
- [12] S. Welte, B. Hacker, S. Daiss, S. Ritter, and G. Rempe, Cavity Carving of Atomic Bell States, *Phys. Rev. Lett.* **118**, 210503 (2017).
- [13] I. D. Leroux, M. H. Schleier-Smith, and V. Vuleti , Implementation of Cavity Squeezing of a Collective Atomic Spin, *Phys. Rev. Lett.* **104**, 073602 (2010).
- [14] M. H. Schleier-Smith, I. D. Leroux, and V. Vuleti , States of an Ensemble of Two-Level Atoms with Reduced Quantum Uncertainty, *Phys. Rev. Lett.* **104**, 073604 (2010).
- [15] J. Ma, X. Wang, C. P. Sun, and F. Nori, Quantum spin squeezing, *Physics Reports* **509**, 89 (2011).
- [16] O. Hosten, N. J. Engelsen, R. Krishnakumar, and M. A. Kasevich, Measurement noise 100 times lower than the quantum-projection limit using entangled atoms, *Nature* **529**, 505 (2016).
- [17] L. Pezz , A. Smerzi, M. K. Oberthaler, R. Schmied, and P. Treutlein, Quantum metrology with nonclassical states of atomic ensembles, *Rev. Mod. Phys.* **90**, 035005 (2018).
- [18] K. Baumann, C. Guerlin, F. Brennecke, and T. Esslinger, Dicke quantum phase transition with a superfluid gas in an optical cavity, *Nature* **464**, 1301 (2010).
- [19] R. M. Kroeze, Y. Guo, V. D. Vaidya, J. Keeling, and B. L. Lev, Spinor Self-Ordering of a Quantum Gas in a Cavity, *Phys. Rev. Lett.* **121**, 163601 (2018).
- [20] J. A. Muniz, D. Barberena, R. J. Lewis-Swan, D. J. Young, J. R. K. Cline, A. M. Rey, and J. K. Thompson, Exploring dynamical phase transitions with cold atoms in an optical cavity, *Nature* **580**, 602 (2020).
- [21] A. Periwal, E. S. Cooper, P. Kunkel, J. F. Wienand, E. J. Davis, and M. Schleier-Smith, Programmable interactions and emergent geometry in an array of atom clouds, *Nature* **600**, 630 (2021).
- [22] D. N. Basov, A. Asenjo-Garcia, P. J. Schuck, X. Zhu, and A. Rubio, Polariton panorama, *Nanophotonics* **10**, 549 (2020).
- [23] M. Tavis and F. W. Cummings, Exact Solution for an N -Molecule—Radiation-Field Hamiltonian, *Phys. Rev.* **170**, 379 (1968).

- [24] E. Orgiu, J. George, J. A. Hutchison, E. Devaux, J. F. Dayen, B. Doudin, F. Stellacci, C. Genet, J. Schachenmayer, C. Genes, G. Pupillo, P. Samorì, and T. W. Ebbesen, Conductivity in organic semiconductors hybridized with the vacuum field, *Nature Mater* **14**, 1123 (2015).
- [25] J. Schachenmayer, C. Genes, E. Tignone, and G. Pupillo, Cavity-Enhanced Transport of Excitons, *Phys. Rev. Lett.* **114**, 196403 (2015).
- [26] C. Gonzalez-Ballester, J. Feist, E. Gonzalo Badía, E. Moreno, and F. J. Garcia-Vidal, Uncoupled Dark States Can Inherit Polaritonic Properties, *Phys. Rev. Lett.* **117**, 156402 (2016).
- [27] T. Botzung, D. Hagenmüller, S. Schütz, J. Dubail, G. Pupillo, and J. Schachenmayer, Dark state semilocalization of quantum emitters in a cavity, *Phys. Rev. B* **102**, 144202 (2020).
- [28] N. C. Chávez, F. Mattiotti, J. A. Méndez-Bermúdez, F. Borgonovi, and G. L. Celardo, Disorder-Enhanced and Disorder-Independent Transport with Long-Range Hopping: Application to Molecular Chains in Optical Cavities, *Phys. Rev. Lett.* **126**, 153201 (2021).
- [29] F. Mivehvar, F. Piazza, T. Donner, and H. Ritsch, Cavity QED with quantum gases: New paradigms in many-body physics, *Advances in Physics* **70**, 1 (2021).
- [30] R. Houdré, R. P. Stanley, and M. Illegems, Vacuum-field Rabi splitting in the presence of inhomogeneous broadening: Resolution of a homogeneous linewidth in an inhomogeneously broadened system, *Phys. Rev. A* **53**, 2711 (1996).
- [31] Z. Kurucz, J. H. Wesenberg, and K. Mølmer, Spectroscopic properties of inhomogeneously broadened spin ensembles in a cavity, *Phys. Rev. A* **83**, 053852 (2011).
- [32] I. Diniz, S. Portolan, R. Ferreira, J. M. Gérard, P. Bertet, and A. Auffèves, Strongly coupling a cavity to inhomogeneous ensembles of emitters: Potential for long-lived solid-state quantum memories, *Phys. Rev. A* **84**, 063810 (2011).
- [33] S. Putz, D. O. Krimer, R. Amsüss, A. Valookaran, T. Nöbauer, J. Schmiedmayer, S. Rotter, and J. Majer, Protecting a spin ensemble against decoherence in the strong-coupling regime of cavity QED, *Nature Phys* **10**, 720 (2014).
- [34] J. D. Breeze, E. Salvadori, J. Sathian, N. M. Alford, and C. W. M. Kay, Room-temperature cavity quantum electrodynamics with strongly coupled Dicke states, *npj Quantum Inf* **3**, 40 (2017).
- [35] D. M. Lukin, A. D. White, R. Trivedi, M. A. Guidry, N. Morioka, C. Babin, Ö. O. Soykal, J. Ul-Hassan, N. T. Son, T. Ohshima, P. K. Vasireddy, M. H. Nasr, S. Sun, J.-P. W. MacLean, C. Dory, E. A. Nanni, J. Wrachtrup, F. Kaiser, and J. Vučković, Spectrally reconfigurable quantum emitters enabled by optimized fast modulation, *npj Quantum Information* **6**, 1 (2020).
- [36] I. Craiciu, I. Craiciu, I. Craiciu, M. Lei, M. Lei, J. Rochman, J. Rochman, J. G. Bartholomew, J. G. Bartholomew, J. G. Bartholomew, J. G. Bartholomew, A. Faraon, and A. Faraon, Multifunctional on-chip storage at telecommunication wavelength for quantum networks, *Optica, OPTICA* **8**, 114 (2021).
- [37] S. D. Mishra, R. Trivedi, A. H. Safavi-Naeini, and J. Vučković, Control Design for Inhomogeneous-Broadening Compensation in Single-Photon Transducers, *Phys. Rev. Applied* **16**, 044025 (2021).
- [38] A. D. White, R. Trivedi, K. Narayanan, and J. Vučković, Enhancing Superradiance in Spectrally Inhomogeneous Cavity QED Systems with Dynamic Modulation, *ACS Photonics* **9**, 2467 (2022).
- [39] D. Hunger, T. Steinmetz, Y. Colombe, C. Deutsch, T. W. Hänsch, and J. Reichel, A fiber Fabry–Perot cavity with high finesse, *New J. Phys.* **12**, 065038 (2010).
- [40] S. Garcia, F. Ferri, K. Ott, J. Reichel, and R. Long, Dual-wavelength fiber Fabry–Perot cavities with engineered birefringence, *Opt. Express* **26**, 22249 (2018).
- [41] S. Garcia, F. Ferri, J. Reichel, and R. Long, Overlapping two standing waves in a microcavity for a multi-atom photon interface, *Opt. Express* **28**, 15515 (2020).
- [42] F. Ferri, S. Garcia, M. Baghdad, J. Reichel, and R. Long, Mapping optical standing-waves of an open-access Fabry–Perot cavity with a tapered fiber, *Review of Scientific Instruments* **91**, 033104 (2020).
- [43] J. P. Brantut, J. F. Clément, M. R. de Saint Vincent, G. Varoquaux, R. A. Nyman, A. Aspect, T. Bourdel, and P. Bouyer, Light-shift tomography in an optical-dipole trap for neutral atoms, *Phys. Rev. A* **78**, 031401 (2008).
- [44] J. Dubail, T. Botzung, J. Schachenmayer, G. Pupillo, and D. Hagenmüller, Large random arrowhead matrices: Multifractality, semilocalization, and protected transport in disordered quantum spins coupled to a cavity, *Phys. Rev. A* **105**, 023714 (2022).
- [45] L. W. Clark, N. Jia, N. Schine, C. Baum, A. Georgakopoulos, and J. Simon, Interacting Floquet polaritons, *Nature* **571**, 532 (2019).
- [46] I. Shlesinger, P. Senellart, P. Senellart, L. Lanco, L. Lanco, J.-J. Greffet, and J.-J. Greffet, Time-frequency encoded single-photon generation and broadband single-photon storage with a tunable subradiant state, *Optica, OPTICA* **8**, 95 (2021).
- [47] A. Piñeiro Orioli, J. K. Thompson, and A. M. Rey, Emergent Dark States from Superradiant Dynamics in Multi-level Atoms in a Cavity, *Phys. Rev. X* **12**, 011054 (2022).
- [48] M. Lei, R. Fukumori, J. Rochman, B. Zhu, M. Endres, J. Choi, and A. Faraon, Many-body cavity quantum electrodynamics with driven inhomogeneous emitters, (2022), arXiv:2208.04345.
- [49] D. Barredo, S. de Léséleuc, V. Lienhard, T. Lahaye, and A. Browaeys, An atom-by-atom assembler of defect-free arbitrary two-dimensional atomic arrays, *Science* **354**, 1021 (2016).
- [50] M. Endres, H. Bernien, A. Keesling, H. Levine, E. R. Anschuetz, A. Krajenbrink, C. Senko, V. Vuletic, M. Greiner, and M. D. Lukin, Atom-by-atom assembly of defect-free one-dimensional cold atom arrays, *Science* **354**, 1024 (2016).
- [51] E. Deist, J. A. Gerber, Y.-H. Lu, J. Zeiher, and D. M. Stamper-Kurn, Superresolution Microscopy of Optical Fields Using Tweezer-Trapped Single Atoms, *Phys. Rev. Lett.* **128**, 083201 (2022).
- [52] N. Sauerwein, F. Orsi, P. Uhrich, S. Bandyopadhyay, F. Mattiotti, T. Cantat-Moltrecht, G. Pupillo, P. Hauke, and J.-P. Brantut, Engineering random spin models with atoms in a high-finesse cavity, (2022), arXiv:2208.09421.
- [53] F. Ferri, A. L. Rooij, C. Leboutteiller, P.-A. Bourdel, M. Baghdad, S. Schwartz, S. Garcia, J. Reichel, and R. Long, An optical elevator for precise delivery of cold atoms using an acousto-optical deflector, *New J. Phys.* **24**, 043013 (2022).
- [54] J. R. Johansson, P. D. Nation, and F. Nori, *QuTiP 2*:

- A Python framework for the dynamics of open quantum systems, *Computer Physics Communications* **184**, 1234 (2013).
- [55] B. Arora, M. S. Safronova, and C. W. Clark, Magic wavelengths for the $n\text{p}\rightarrow n\text{s}$ transitions in alkali-metal atoms, *Phys. Rev. A* **76**, 052509 (2007).
 - [56] F. Le Kien, P. Schneeweiss, and A. Rauschenbeutel, Dynamical polarizability of atoms in arbitrary light fields: General theory and application to cesium, *Eur. Phys. J. D* **67**, 92 (2013).
 - [57] C. Gardiner and P. Zoller, *Quantum Noise: A Handbook of Markovian and Non-Markovian Quantum Stochastic Methods with Applications to Quantum Optics*, 3rd ed., Springer Series in Synergetics (Springer-Verlag, Berlin Heidelberg, 2004).
 - [58] C. K. Law, S.-Y. Zhu, and M. S. Zubairy, Modification of a vacuum Rabi splitting via a frequency-modulated cavity mode, *Phys. Rev. A* **52**, 4095 (1995).

METHODS

Experimental setup

At the core of our experimental setup lies a high-finesse fiber Fabry-Perot optical microcavity with a length of $140\text{ }\mu\text{m}$. The maximum single atom coupling strength is $g_0/2\pi \simeq 76\text{ MHz}$, larger than the cavity decay rate $\kappa/2\pi \simeq 15\text{ MHz}$ and the spontaneous emission rate $\gamma/2\pi \simeq 3\text{ MHz}$ (κ and γ are HWHM values), so that we operate in the strong coupling regime of CQED at the single atom level. To realize a homogeneous and maximal coupling of all atoms with the cavity mode, the atoms are trapped at the antinodes of the cavity mode which is resonant with the D2 line of ^{87}Rb at 780 nm (see Fig. 1 in the main text). We achieve this condition by using an intracavity standing wave at a wavelength of 1559 nm , commensurate with the atomic line taking into account the Gouy phase shift and by optimizing the phase shift at reflection on the mirrors [41, 42] such that the antinodes of both 1559 nm and 780 nm standing waves overlap optimally.

To load the atoms into the cavity, we start with a 3D magneto-optical trap (MOT) of Rubidium atoms positioned 12 mm below the cavity and loaded by a 2D-MOT. The atoms are then trapped inside a horizontal dipole beam that we can displace vertically with an acousto-optical deflector [53]. In 100 ms , the atoms are moved into the cavity. To load the atoms into the one dimensional intracavity lattice, we increase the 1559 nm intracavity power while decreasing the intensity of the transport beams. We can adjust the number of atoms from a few tens up to 2000 by varying the loading parameters of the MOT. The atoms are first trapped in a $300\text{ }\mu\text{K}$ deep intracavity lattice at a temperature of $50\text{ }\mu\text{K}$. We can then increase the trap depth by performing an adiabatic compression of the cloud.

Atomic frequency distributions probed by loss spectroscopy

The strong frequency broadening in our experiment results from the combination of finite atomic temperature, lightshifts and level mixing effects described in the Supplementary Information. To characterize the frequency distribution of the atoms, we measure the losses of the atom ensemble (prepared in the $F = 2$ hyperfine ground state) induced by a probe beam perpendicular to the cavity axis. This beam is switched on for 0.5 ms at a given frequency before performing the loss measurement. We repeat this process for frequencies values across the distribution. To obtain reliable atom number measurements down to low atom numbers, the loss measurement is performed by measuring the vacuum Rabi splitting of the cavity transmission signal (see section Cavity Transmission Spectrum). The results are shown on Fig. 1.

Because the atoms are excited with uncontrolled phases and amplitudes by this transverse beam, we expect (and observe) negligible coupling between the latter and the bright modes of the coupled atom-cavity system even though the resonance condition is fulfilled.

To generate the simulated frequency distribution curves shown on Fig. 1c, we assume that the atoms are in thermal equilibrium at each site of the optical lattice, described by an harmonic trap with radial frequencies $\omega_x = \omega_y$ and longitudinal frequency ω_z . For a trap depth of 1.40 mK , $\omega_{x,y}/2\pi = 14.5\text{ kHz}$, and $\omega_z/2\pi = 330\text{ kHz}$. For each atom of a given sample, we first draw x , y and z from a normal distribution with variance $\sigma_{x,y,z}^2 = k_B T / (m\omega_{x,y,z}^2)$. Then we deduce the values of the coupling $g(x, y, z)$ (based on the cavity parameters) and of the dipole trap intensity $I_{dip}(x, y, z)$ (based on the maximum value at the bottom of the trap, which is estimated from lightshift measurements and corroborated by a direct transmission measurement). The intensity $I_{dip}(x, y, z)$ seen by each atom is used to construct a 16×16 matrix representing the Stark operator in the $|F, m_F\rangle$ basis of the $5P_{3/2}$ manifold (see Supplementary Information). The output of the procedure for N atoms is a collection of $16 \times N$ eigenvalues $\hbar\omega_{k,j}$ and eigenvectors $|\psi_{k,j}\rangle$, where $1 \leq j \leq 16$ and $1 \leq k \leq N$.

In addition, we assume that the initial atomic population is equally distributed between all Zeeman sublevels of the $F = 2$ hyperfine ground state. For each atom (labelled by the index k), we use the previous procedure to compute the 5×16 transition frequencies $\omega_{k,j}(m_F)$ between the 5 ground states $|F = 2, m_F\rangle$ and the 16 excited states $|\psi_{k,j}\rangle$ (with $-2 \leq m_F \leq 2$ and $1 \leq j \leq 16$). Each frequency $\omega_{k,j}(m_F)$ is associated to a coupling strength $c_{k,j}(m_F)$, defined as:

$$c_{k,j}(m_F) = \left| \left\langle \psi_{k,j} \left| \sum_{q=-1}^1 \hat{d}_q E_q^t \right| F = 2, m_F \right\rangle \right|^2, \quad (3)$$

where E_q^t are the components of the electric field of the probe beam \mathbf{E}^t , expressed in the spherical basis and \hat{d}_q are the dipole matrix elements (see Supplementary Material). In the experiment, we have $E_0^t/|\mathbf{E}^t| = 1/\sqrt{2}$ and $E_{\pm 1}^t/|\mathbf{E}^t| = \pm 1/2$. The frequency distributions shown on Fig. 1c are then obtained by sorting the transition frequencies $\omega_{k,j}(m_F)$ in equal-width bins, weighted by their coupling strength $c_{k,j}(m_F)$. For a given trap depth, we use an effective temperature T (2 to 3 times the initial experimental temperature) to match the positions of the simulated and experimental curves. The discrepancy stems from heating and depumping effects induced by the transverse beam. The amplitude of each curve is adjusted such that they all have the same area.

Cavity Transmission Spectrum

Data acquisition

To measure the cavity transmission spectrum, we first prepare the atoms in the $|F = 2, m_F = 2\rangle$ Zeeman sublevel by optical pumping. The trap depth is $1400 \pm 30 \mu\text{K}$ and the temperature $190 \pm 20 \mu\text{K}$. To ensure that no atom remains in other sublevels, we furthermore apply the following sequence: microwave transfer to $|F = 1, m_F = 1\rangle$, blast of the remaining atoms in the $|F = 2\rangle$ hyperfine level and microwave transfer back to $|F = 2, m_F = 2\rangle$. We estimate that ≈ 800 atoms are in the $|F = 2, m_F = 2\rangle$ state at the end of the preparation sequence. We then probe the cavity-atoms coupled system by sweeping a tunable laser over a range of 8 GHz in 8 ms. Its intensity is chosen such that the average photon number in the cavity is smaller than unity ($\langle n_{\text{cav}} \rangle = 0.14$), to be in low excitation limit. We measure the transmitted light with a single-photon counting module. To calibrate the frequency axis of the spectrum, we record simultaneously the transmission signal of a 10 cm long cavity providing a frequency ruler allowing us to compensate the slight non-linearity of the frequency sweep, and a saturated absorption signal of the probe laser that provides an absolute frequency reference. We estimate the uncertainty of the frequency of the probe laser to be ± 8 MHz (1 standard deviation), well below the Rabi splittings of typically 100 to 4000 MHz.

As the single-shot spectra are strongly discretized (see Fig. E2), we average ≈ 200 such spectra to obtain the experimental data shown on Fig. 2. As experimental fluctuations of N result into fluctuations of the collective coupling, we group and average the spectra according to their collective coupling Ω to avoid excessive broadening due to averaging. We used a 40 MHz bin centered on $\Omega/2\pi = 1670$ MHz, to maximize the number of spectra in the bin. We fit independently the high and low frequency peaks of the averaged spectrum with a Voigt profile to extract the half-width at half-maximum (HWHM) of the peaks. The HWHM width ($\delta\omega_-/2\pi = 28 \pm 2$ MHz) of the low frequency peaks is a bit larger than the one of the high frequency peak ($\delta\omega_+/2\pi = 24 \pm 2$ MHz), probably due to the presence of atom losses during the measurement. The HWHM value quoted in the main text ($\delta\omega/2\pi = 26 \pm 2$ MHz) is the average of the experimental polarizations' widths.

Simulation of the transmission spectrum and frequency distribution

For a given atom k , the excited subspace of the $5P_{3/2}$ manifold dressed by the dipole light features 16 eigenvalues $\hbar\omega_{k,j}$ and the 16 corresponding eigenstates $|\psi_{k,j}\rangle$, where $1 \leq k \leq N$ enumerates the atoms and $1 \leq j \leq 16$

the eigenstates of the excited subspace. The cavity is probed with a weak pulse of σ_+ polarized light which couples the ground state $|k : 2, 2\rangle$ of atom number k to $|k : 3, 3\rangle$, the $|5P_{3/2}, F' = 3, m_{F'} = 3\rangle$ Zeeman sublevel of this atom. The coherent evolution is described by a multilevel version of the standard Tavis-Cummings Hamiltonian (see Supplementary Information). Taking into account photon losses κ and atomic decay γ , the transmission of the cavity as a function of the probe frequency ω , is given by the following simple analytical form, that was derived in [32] using the input-output formalism:

$$t(\omega) = \frac{-\kappa/(2i)}{\omega_c - i\kappa/2 - \omega - \sum_{k,j} \frac{(g_{k,j})^2}{\omega_{k,j} - i\gamma/2 - \omega}}. \quad (4)$$

To simulate the averaged spectrum of Fig. 2, we compute many transmission spectra with a trap depth $U_0 = 1400 \mu\text{K}$ and a temperature $T = 190 \mu\text{K}$. We draw randomly the number of atoms N , to account for experimental fluctuations. We average single spectra (≈ 350) featuring a collective coupling within the bin 1670 ± 28 MHz. This corresponds to the bin chosen for the experimental spectra of Fig. 2, enlarged by ± 8 MHz to account for the 1-standard deviation uncertainty on frequencies of the spectrum. For the spectral distribution, we reconstruct the spectral distribution of couplings $\rho(\omega) = \sum_{k=1}^N \sum_{j=1}^{16} g_{k,j}^2 \delta(\omega - \omega_{k,j})$ by drawing $N = 100\,000$ random atomic positions and computing the associated distribution of $(\omega_{k,j}, g_{k,j})$. We then sort the transition frequencies $\omega_{k,j}$ in equal-width bins, weighted by their coupling strength $|g_{k,j}|^2$. The calculated distributions are shown on Fig. E1 for various values of the trap depth U_0 , and on Fig. 2 ($U_0 = 1040 \mu\text{K}$) together with the corresponding transmission spectrum.

Transition from the unprotected to the cavity-protected regime for a finite-sized system

Data acquisition

To explore the transition from the unprotected to the cavity-protected regime, we acquire ~ 2000 experimental spectra for an increasing number of atoms N (from ~ 10 to 550). Experimentally we tune N by varying the loading time of our magneto-optical-trap. The trap depth is $U_0 = 1040 \pm 30 \mu\text{K}$ and the temperature is $T = 140 \pm 20 \mu\text{K}$. The cavity frequency is set equal to the average frequency of the corresponding coupling distribution $\rho(\omega)$ (red distribution in Fig 1.): $\omega_c = \omega_{|2,2\rangle \rightarrow |3,3\rangle} - 970$ MHz (we justify this choice for ω_c in Supplementary Information section II.2). For each experimental spectrum, we compute the collective coupling Ω as the distance between the central frequencies ω_{\pm} of each half of the spectrum. ω_{\pm} is defined as the barycenter

of the photon-count distribution within a half-spectrum. This definition does not rely on a fit and allows computing Ω even for multi-peak spectra in the unprotected regime.

As the average number of photons inside the cavity is much lower than one, the number of photons collected is low and the spectrum is strongly discretized as shown in Fig.E2, preventing us from directly extracting the PW of eigenstates exhibiting a low transmission. So, we characterize the degree of coherence of the system by measuring the fraction F_{out} of photon counts outside a frequency range $\Delta f/2\pi$, in which most of the counts lay in the protected regime. First, we define the typical frequency width $\Delta f/2\pi$ of the polariton peak in the cavity-protected regime (for $\Omega/2\pi \geq 1000$ MHz) as twice the standard deviation σ of the photon-count weighted frequency distribution. In this regime, we measure $\Delta f/2\pi = 140$ MHz and $\approx 90\%$ of the counts are within Δf . Then we separate the spectrum into two halves at the cavity frequency ω_c . For each half of the spectrum (\pm), we compute the total number of counts $N_{tot,\pm}$, the mean value Ω_{\pm} of the frequency distribution of the spectrum (weighted by the counts) and the number of counts $N_{out,\pm}$ that are outside the intervals $[\Omega_{\pm} - \Delta f/2; \Omega_{\pm} + \Delta f/2]$. Finally, we compute the fractions of counts outside of these intervals, $F_{out,\pm}$ (respectively F_{out}), for the two halves of the spectrum (respectively the total spectrum). For F_{out} , we get a cloud of points (Ω, F_{out}) , which we average with 30 MHz-bins of Ω . Vertical error bars are equal to $\pm \frac{\sigma}{\sqrt{N_p}}$, where σ is the standard deviation of the N_p points gathered within a bin. The resulting curve is plotted in the Fig. 3. We have also checked that F_{out} is robust with respect to the exact value of $\Delta f/2\pi$, as shown in Fig. E3).

Calculation of S_{PW}

Operating in the strong coupling regime at the single atom level enables us to explore the transition from the unprotected to the protected regime for a mesoscopic number of atoms ranging from 10 to 550. For such numbers of emitters, we are far from the continuous frequency distribution of emitters usually encountered in solid-state systems and are sensitive to the finite size of the Hilbert space and to the discreteness of the spectrum of the coupled emitters-cavity system. In particular, we can directly compute the eigenvalues and eigenvectors of the coupled system and extract their properties.

In the low excitation limit, we restrict the dynamics of the closed system to the one excitation manifold. For N two-level atoms, it is spanned by the $N + 1$ basis states $\{|1, G\rangle, |0, E_1\rangle, \dots, |0, E_k\rangle, \dots, |0, E_N\rangle\}$ with $|G\rangle = |g_1 \dots g_N\rangle$ and $|E_k\rangle = |g_1 \dots e_k \dots g_N\rangle$, where $|g_k\rangle$ (resp. $|e_k\rangle$) is the ground (resp. excited) state of the

atom k .

Due to the 1559 nm trapping light, a given atom k is excited to the subspace of the $5P_{3/2}$ manifold featuring 16 eigenvalues $\omega_{k,j}$ and eigenstates $|\psi_{k,j}\rangle$. The single excitation manifold is then spanned by the $16 \times N + 1$ basis states $\{|1, G\rangle, |0, E_{1,1}\rangle, \dots, |0, E_{k,j}\rangle \dots |0, E_{N,16}\rangle\}$ where $|G\rangle = |G_1, \dots, G_k, \dots, G_N\rangle$ with $|G_k\rangle = |g_{k,1} \dots g_{k,j} \dots g_{k,16}\rangle$ and $|E_{k,j}\rangle = |G_1, \dots, g_{k,1} \dots \psi_{k,j} \dots g_{k,16}, \dots, G_N\rangle$.

In this basis, the Tavis-Cummings Hamiltonian for multilevel atoms is given by an arrowhead matrix, from which we can numerically extract the $D = 16 \times N + 1$ eigenstates Ψ_i^C and eigenvalues ε_i ($i = 1, \dots, D$) of the atoms - cavity coupled system. We can then compute the photonic weight of the eigenstates Ψ_i^C defined as the weight of the $|1, G\rangle$ component:

$$PW_i = |\langle 1, G | \Psi_i^C \rangle|^2$$

To simulate the theoretical curve of Fig. 3, we draw N_{atom} random atomic positions (where N_{atom} is the atom number), deduce the associated values of frequencies and cavity couplings $(\omega_{k,j}, g_{k,j})$ and compute the PW of the different eigenstates. We then calculate S_{PW} which we have defined as the sum of all photonic weights except the two largest ones: $S_{PW} = 1 - PW_{max1} - PW_{max2}$. For each value of N_{atom} , we average S_{PW} over 300 repetitions.

Polariton Modulation

Data acquisition

To modulate the polaritons, we modulate the average light-shifted frequency of the atoms $\bar{\omega}_A(t) = \bar{\omega}_A^0 + \beta_o \omega_m \cos(\omega_m t)$ where β_o is the modulation index, by modulating the intracavity dipole power at a frequency $\omega_m/2\pi$. The spectrum of Fig. 4 is obtained by averaging ≈ 200 spectra. Before averaging, we select spectra with similar atom number N , by measuring the dispersive shift $\delta\omega_c$ of the cavity frequency when the atoms are in the state $|F = 1, m_F = 1\rangle$, which is given by:

$$\delta\omega_c = \frac{-N g_{|2,2\rangle \rightarrow |3,3\rangle}^2}{2(\omega_{|1,1\rangle \rightarrow |2,2\rangle} - \omega_c)} \quad (5)$$

We select spectra within the dispersive shift bin $\delta\omega_c/2\pi = -258 \pm 5$ MHz, corresponding to $N = 1130 \pm 25$ or to collective coupling $\Omega/2\pi = 2020 \pm 20$ MHz. The trap depth is $1400 \mu\text{K}$ and the temperature is $190 \mu\text{K}$, similar to the data of main text Fig. 2. The modulation frequency is $\omega_m/2\pi = 120$ MHz.

As we are in the regime where $\Omega \gg \omega_m$, the cavity spectrum is given by the following expression, derived in

Supplementary Information (equation 25.):

$$S(\omega) \propto \sum_n \frac{J_n^2(\beta_o/2)}{(\omega - \omega_0 - n\omega_m + \Omega)^2 + \gamma_s^2} + \sum_n \frac{J_n^2(\beta_o/2)}{(\omega - \omega_0 - n\omega_m - \Omega)^2 + \gamma_s^2} \quad (6)$$

The cavity spectrum features two combs of peaks centered at $\pm\Omega$. The separation between two consecutive peaks is given by the modulation frequency ω_m . The amplitude of each peak is given by $J_n^2(\beta_o/2)$ and so the modulation index for the polaritons is given by $\beta_p = \beta_o/2$. We are then able to directly control the modulation of the polaritons in frequency and amplitude with the modulation of the trapping light. The width of each peak is given by $\gamma_s = \frac{\kappa + \gamma}{2}$, identical to the width of the non-modulated homogeneous case as we are in the cavity protected regime. As the number of atoms inside the cavity modes fluctuates, the transmission peak of the high frequency polariton is best-fitted by Voigt function:

$$\sum_n J_n^2(\beta_p) \text{Voigt}(\omega - \omega_0 - n\omega_m \pm \Omega, \gamma_s, \sigma) \quad (7)$$

where $\text{Voigt}((\omega, \gamma_s, \sigma) = \frac{1}{\sqrt{2\pi}\sigma} \Re(\text{wofz}(\frac{\omega + i\gamma_s}{\sqrt{2}\sigma}))$ with wofz the Faddeeva function. This function provides a very good fit of the experimental data, except for the slight asymmetric shape (relative variation of $\pm 7\%$) between the right and left part of each comb.

Simulation of the cavity transmission spectra

To justify the function used to fit the experimental data and to confirm the analysis presented in the Supplementary Information, we simulate the cavity spectrum by numerically integrating the master equation using Qutip [54], for an emitter-cavity system probed by a laser swept in frequency at the same rate as in the experiment (1 GHz/ms), and with the same power. We calculate the population of the state $|1, G\rangle$ after binning

the simulated results to match the experimental resolution of 2.5 MHz. By using the parameters given by the experimental fit, we obtain a very good agreement between the experimental data and the simulated spectra even for the asymmetrical shape of the comb.

Modulation transfer measurement

To measure the linear modulation transfer $\beta_p \propto \beta_o$ (inset of Fig. 4), we measure ≈ 100 spectra for each value of β_o . We reduce the frequency range of the probe laser scan by a factor of 4 to increase the frequency resolution. Before averaging spectra, we frequency-shift each spectrum so that the multi-peaks centers of all spectra are aligned, to compensate for atom number fluctuations. Compared to a raw averaging, this technique improves the accuracy of the relative amplitudes of the different peaks in the average spectrum, to which the value of β_p is very sensitive. We then fit the cavity spectrum with the function (5) to extract the value of β_p .

Since β_p is the result of a non-linear fit, we resort to a nonparametric bootstrap method to determine its uncertainty. For each averaged spectrum (and thus each value of β_p), we generate 500 synthetic spectra A_k ($1 \leq k \leq 500$). Then, each synthetic spectrum A_k is fitted with the formula (5), providing a fitted parameter $\beta_{p,k}$. The errorbar for β_p is defined as the \pm the standard deviation of the set $\{\beta_{p,k} ; 1 \leq k \leq 500\}$. To obtain the value of β_o , we measure the intensities of the different frequency components of the trapping light, using the transmission spectrum of the frequency-scanned cavity. Starting from $\delta\omega_a(t) = \overline{\omega_A}(t) - \overline{\omega_A^0} = \beta_o\omega_m\cos(\omega_mt)$, we get:

$$\beta_o = \frac{\delta\omega_a^{max}}{\omega_m} = \frac{|\overline{\omega_A^0}|}{\omega_m} \frac{\delta\omega_a^{max}}{|\overline{\omega_A^0}|} = \frac{|\overline{\omega_A^0}|}{\omega_m} \frac{\delta I_D^{max}}{I_D^0} \quad (8)$$

where $\overline{\omega_A^0}/2\pi = -1320$ MHz is the average atomic light-shift, $\omega_m/2\pi = 130$ MHz is the modulation frequency, and I_D^0 and δI_D^{max} are, respectively, the constant and ω_m frequency-dependent components of the intensity of the trapping light. Uncertainties on β_o are propagated from the experimental uncertainties of ω_a^0 , I_D^0 and δI_D^{max} .

EXTENDED DATA

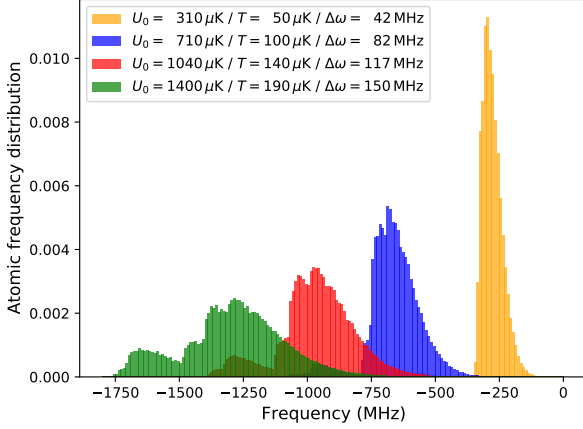


FIG. E1. **Simulated atomic frequency distribution for different trap depths.** For each trap depth U_0 , the temperature T used in the simulation corresponds to the typical experimental value based on time-of-flight measurements. When U_0 increases, the mean frequency of the distribution decreases linearly – as expected with red-detuned off-resonant light – and the width $\Delta\omega$ of the distribution increases. At low trap depth $U_0 = 310 \pm 10 \mu\text{K}$ the distribution has mainly one lobe, corresponding to the $|F = 2\rangle \rightarrow |F' = 3\rangle$ transition. For larger trap depths, two-photon couplings at 1559nm mix the excited state hyperfine levels and two extra lobes appear in the distributions, at lower frequencies, corresponding roughly to transitions $|F = 2\rangle \rightarrow |F' = 2\rangle$ and $|F = 2\rangle \rightarrow |F' = 1\rangle$. This illustrates the tunability of the inhomogeneous distribution with the intensity of the trapping field.

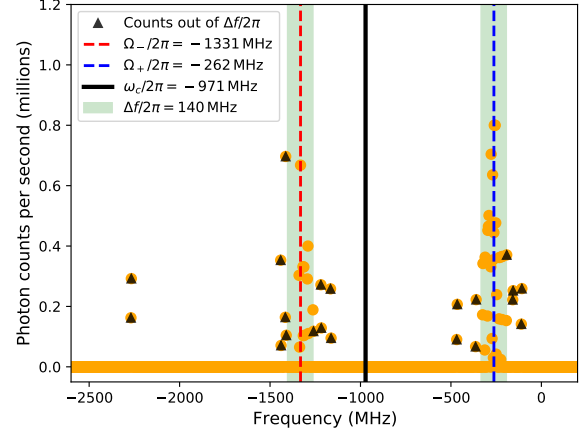


FIG. E2. **Single shot experimental spectrum.** As we probe the coupled system in the low excitation regime, we collect few photons in transmission and the spectrum is discretized (orange dots). For each spectrum, we compute the fraction F_{out} of photons (identified with black triangles) that lies outside of a frequency window $\Delta f/2\pi$ (green colored area), centered on each peak distribution (red and blue dashed lines).

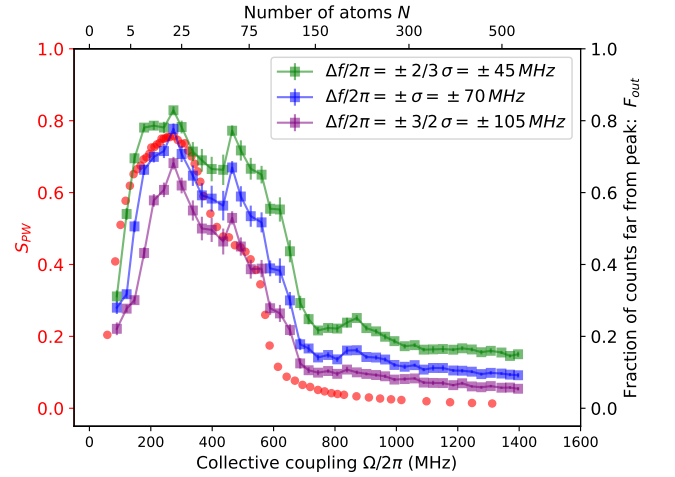


FIG. E3. **Robustness of F_{out} with respect to the size of the exclusion window.** Here we show F_{out} for several values of $\Delta f/2\pi$ chosen to define the exclusion window, together with the simulated sum of the two highest photonic weight, S_{PW} , as in Fig. 3 of the main text (red dots). The result is rather robust: when $\delta f/2\pi$ decreases, the shape of F_{out} remains the same, and is shifted upwards as expected.

SUPPLEMENTARY INFORMATION

EFFECT OF THE 1559 NM LIGHT ON THE $5P_{3/2}$ MANIFOLD

Following [55, 56], we describe the combined effects of lightshifts and level mixing within the $5P_{3/2}$ manifold induced by the 1559 nm light by a Stark operator \hat{V} , whose matrix elements in the $|F, m_F\rangle$ basis are given by:

$$\langle F', m'_F | \hat{V} | F, m_F \rangle = \sum_{|k\rangle} \frac{\langle F', m'_F | \hat{\mathbf{d}} \cdot \mathbf{E} | k \rangle \langle k | \hat{\mathbf{d}} \cdot \mathbf{E} | F, m_F \rangle}{-\hbar \Delta_k} \quad (9)$$

where Δ_k is defined as:

$$\frac{1}{\Delta_k} = \frac{1}{(\omega_k - \omega_{5P_{3/2}}) - \omega} + \frac{1}{(\omega_k - \omega_{5P_{3/2}}) + \omega},$$

all relevant states $|k\rangle$ being much farther in energy than the hyperfine splitting. In our case, given the value of the reduced matrix element and the detuning from the 1559 nm light of each atomic line [55], we expect most ($> 99\%$) of the contribution in the sum of equation (9) to result from $4D_{5/2}$, $4D_{3/2}$, $6S_{1/2}$ and $5S_{1/2}$, so we keep only these lines in the simulations.

To compute the matrix elements $\langle F', m'_F | \hat{\mathbf{d}} \cdot \mathbf{E} | F, m_F \rangle$ for a given atomic line and quantization axis \mathbf{e}_z , we express the electric field of the 1559 nm trapping light $\mathbf{E} = (E_x, E_y, E_z)$ in the spherical basis:

$$\mathbf{E} = \sum_{q=-1,0,1} E_q \mathbf{e}_q, \quad (10)$$

where the \mathbf{e}_q are unitary vectors and the E_q are the “pi” and “sigma” components of \mathbf{E} related to $E_{x,y,z}$ by:

$$E_0 = E_z \quad \text{and} \quad E_{\pm 1} = (\pm E_x + i E_y) / \sqrt{2}.$$

The matrix elements of $\hat{d}_q = \hat{\mathbf{d}} \cdot \mathbf{e}_q$ are then computed using the Wigner-Eckart theorem, and reduced matrix elements taken from reference [55]. In our typical experimental situation, the magnetic field is along the cavity axis z , and the polarization of the trapping light is linear along the x direction, corresponding to $E_0/|\mathbf{E}| = 0$, $E_1/|\mathbf{E}| = 1/\sqrt{2}$ and $E_{-1}/|\mathbf{E}| = -1/\sqrt{2}$.

CAVITY TRANSMISSION SPECTRUM

Inhomogeneous Tavis-Cummings model

The coherent evolution of the coupled atom-cavity system is described by a multilevel version of the standard Tavis-Cummings Hamiltonian (with $\hbar \equiv 1$):

$$H = H_{\text{cav}} + H_{\text{at}} + H_{\text{int}}, \quad (11)$$

where:

- $H_{\text{cav}} = \omega_c a^\dagger a$ is the Hamiltonian of the cavity mode;
- $H_{\text{at}} = \sum_k \sum_j \omega_{k,j} \sigma_{k,j}^+ \sigma_{k,j}^-$ is the Hamiltonian of the multilevel atomic ensemble dressed by the 1559 nm light; the operator $\sigma_{k,j}^+$ is by definition equal to $|\psi_{k,j}\rangle \langle k : 2, 2|$ and $\sigma_{k,j}^- = (\sigma_{k,j}^+)^{\dagger}$;

- $H_{\text{int}} = \sum_k \hbar g_{(k)} (\sigma_k^- a^\dagger + \sigma_k^+ a)$ describes the interaction between the atoms and the cavity mode in the rotating wave approximation, where:

$g_k = g(x_k, y_k, z_k)$ is the coupling constant of the atom k , at the position (x_k, y_k, z_k) , and $\sigma_k^+ = |k : 3, 3\rangle \langle k : 2, 2|$. We can express H_{int} in the following form :

$$H_{\text{int}} = \sum_k \sum_j \left(g_{k,j} \sigma_{k,j}^+ a + g_{k,j} \sigma_{k,j}^- a^\dagger \right)$$

with $g_{k,j} = g_k \langle \psi_{k,j} | k : 3, 3 \rangle$.

In the low excitation limit, where the average photon number inside the cavity is much smaller than unity, the Hilbert space can be reduced to the subspace with one excitation: $\{|1, G\rangle, |0, W\rangle\}$. $|1, G\rangle$ corresponds to the state with one photon in the cavity mode and all atoms in the ground state $|G\rangle = |1 : 2, 2, \dots, N : 2, 2\rangle$. $|0, W\rangle$ is the state with zero photon in the cavity mode and one atomic excitation $|W\rangle = \Sigma^\dagger |G\rangle$, where Σ^\dagger is the collective excitation operator, given by $\Sigma^\dagger = \sum_k \frac{g_k}{\Omega} \sigma_k^+$.

Trap and cavity parameters

Deep into the cavity-protected regime, we observe two transmission peaks separated by twice the collective coupling Ω . By also measuring the number N of atoms in the same sequence using absorption imaging, we have access to the experimental single-atom effective coupling strength $g_{\text{exp}} = \frac{\Omega}{\sqrt{N}}$. In the range of depths and temperatures used in the experiment, we measure coupling strength $g_{\text{exp}}/2\pi$ between 55 and 68 MHz (see Table I). The computed average value g_{sim} of the simulated frequency distribution is in good agreement with the measured data, using the calibration procedure described in the following section for the trap depth U_0 , and time-of-flight measurements of the temperature T .

Cavity detuning and light-shift calibration

In the simple case of a two-level atom with frequency ω_A strongly coupled to a cavity with frequency ω_c , the two polaritons are centered on the frequency $(\omega_A + \omega_c)/2$

TABLE I. Trap and cavity parameters

U (μ K)	T (μ K)	$g_{sim}/2\pi$ (MHz)	$g_{exp}/2\pi$ (MHz)
310 ± 10	50 ± 3	57	56 ± 4
710 ± 20	100 ± 10	60	62 ± 4
1040 ± 30	140 ± 20	60	66 ± 4
1400 ± 30	190 ± 20	60	67 ± 4

[2]. In particular, when the cavity is tuned to resonance with the atomic frequency ($\omega_c = \omega_A$), the center of the transmission doublet coincides with the position of the empty cavity. Our simulations for an inhomogeneous atomic ensemble reveal a similar (and more general) condition: the transmission doublet is centered on the empty cavity when its frequency is equal to the average (lightshifted) atomic frequency, defined by $\bar{\omega}_A = \sum_{k,j} (g_{k,j})^2 \omega_{k,j} / \Omega^2$. To verify this, we simulate, for various atom-cavity detunings, transmission spectra, for $N=500$ atoms, deep in the cavity-protected regime. From each spectrum we extract the central frequency of the Rabi doublet, and average it over 40 realizations. We then fit the average central frequency against detuning with a linear function, which gives us the detuning for which the cavity frequency is at the center of the Rabi doublet. This atom-cavity detuning is compatible

with the average atomic lightshift, computed over 20.000 atoms.

Based on this observation, we experimentally tune the cavity mode frequency to resonance with the average atomic frequency by centering the empty cavity on the transmission doublet in the regime of strong collective coupling. Interestingly, knowing the frequency of the tuned cavity mode provides a precise measurement of the average lightshift, and also of the trap depth based on independent temperature measurements (in practice, we calculate the average lightshift for various trap depths until it coincides with the experimental value up to 1%, which is below the experimental uncertainties). Experimental averaged frequencies $\bar{\omega}_{A,exp}$ are shown in Table II. The values of U_0 are compatible with the measurements performed by direct intensity calibration within the uncertainties margins.

TABLE II. Calibration of trap depth U_0

$\bar{\omega}_A$ (experimental)	T (experimental)	U_0 (simulation)
-280 ± 10 MHz	50 ± 3 μ K	310 ± 10 μ K
-660 ± 10 MHz	100 ± 10 μ K	710 ± 20 μ K
-970 ± 20 MHz	140 ± 20 μ K	1040 ± 30 μ K
-1300 ± 40 MHz	190 ± 20 μ K	1400 ± 30 μ K

POLARITONS MODULATION

Hamiltonian of the modulated atom-cavity system

The data for the polariton modulation have been acquired in the fully protected regime ($\Omega \gg \Delta\omega$). This allows us to consider a simplified model where all atoms have the same atomic frequency $\omega_A(t)$ dressed by the time-dependent 1559 nm dipole light. For this homogeneous system and considering only the low excitation limit, we can restrict the dynamics of the coupled cavity-atoms system to the symmetric subspace of the first excitation manifold spanned by the basis states $\{|1, G\rangle, |0, W\rangle\}$ with $|G\rangle = |g_1 \dots g_N\rangle$ and $|W\rangle = \Sigma^\dagger |G\rangle$, where Σ^\dagger is the collective excitation operator, given by $\Sigma^\dagger = \sum_{k=1}^N \frac{g_k}{\Omega} \sigma_k^+$, with Ω the collective atom-cavity coupling. In this configuration, the $N - 1$ dark states do not play a role in the time evolution of the system. The Hamiltonian of the system is then given by the time-dependent version of the standard Tavis-Cummings Hamiltonian

$$H(t) = \omega_c a^\dagger a + \omega_A(t) \Sigma^\dagger \Sigma + \Omega (\Sigma a^\dagger + \Sigma^\dagger a). \quad (12)$$

By coupling two frequency components of the trapping light within the cavity bandwidth, we produce a beating that induces a modulation of the trapping dipole light at a frequency $\omega_m/2\pi$: $I_D(t) = I_D^0 + \delta I \cos(\omega_m t + \phi)$. This leads to a modulation of the trapping potential $U(t) = U^0 + \delta U \cos(\omega_m t + \phi)$. As this modulation is quite fast in the 100 MHz range, the positions of the atoms in the trap cannot respond to the modulation and we can consider the g coupling distribution is constant. However, the light-shifted atomic frequency is instantaneously modified, and we obtain at first order a modulation $\omega_A(t) = \omega_A^0 + \delta\omega_A(t)$ with $\delta\omega_A(t) = \beta_o \omega_m \cos(\omega_m t + \phi)$, where we define β_o as the "optical" modulation index. The Hamiltonian can then be written as

$$H(t) = \omega_c a^\dagger a + \omega_A^0 \Sigma^\dagger \Sigma + \Omega (\Sigma a^\dagger + \Sigma^\dagger a) + \delta\omega_A(t) \Sigma^\dagger \Sigma. \quad (13)$$

By moving into the rotating frame of the probe laser with frequency ω_p , we can express the Hamiltonian as

$$\tilde{H}(t) = \Delta\omega_c a^\dagger a + \Delta\omega_A^0 \Sigma^\dagger \Sigma + \Omega (\Sigma a^\dagger + \Sigma^\dagger a) + \delta\omega_A(t) \Sigma^\dagger \Sigma, \quad (14)$$

with $\Delta\omega_c = \omega_c - \omega_p$ and $\Delta\omega_A^0 = \omega_A^0 - \omega_p$.

The Hamiltonian is divided into the standard Tavis-Cummings Hamiltonian and a time-dependent perturbation: $\tilde{H}(t) = \tilde{H}_{TS} + \tilde{V}(t)$. The eigenvalues of \tilde{H}_{TS} are given by

$$E_\pm = \frac{\omega_A^0 + \omega_c}{2} - \omega_p \pm \sqrt{\Omega^2 + \left(\frac{\omega_A^0 - \omega_c}{2}\right)^2}. \quad (15)$$

In the following, we consider only the resonant case $\omega_c = \omega_A^0 = \omega_0$. As the frequency modulation $\delta\omega_A(t)$ is small compared to Ω , we express $\tilde{H}(t)$ in the polariton basis $\{|P_+\rangle, |P_-\rangle\}$ of the unmodulated system defined by

$$|P_\pm\rangle = \frac{1}{\sqrt{2}} (|1, G\rangle \pm |0, W\rangle). \quad (16)$$

We obtain

$$\tilde{H}(t) = \begin{pmatrix} \omega_0 - \omega_p + \Omega & 0 \\ 0 & \omega_0 - \omega_p - \Omega \end{pmatrix} + \frac{\delta\omega_A(t)}{2} \begin{pmatrix} 1 & -1 \\ -1 & 1 \end{pmatrix} \quad (17)$$

We see in this expression that the modulation of the emitters frequency modifies the eigenfrequencies of the Tavis-cummings Hamiltonian and also induces a coupling between the two polaritonic states $\{|B_+\rangle, |B_-\rangle\}$, which are not any more the eigenstates of the system.

Analytical expressions

To underline the main physical effect of the modulation, we first consider the situation where initially one excitation is stored in the emitter-cavity system and we calculate the Rabi oscillation and cavity spectrum, which is given by the following relation [57]

$$S(\omega) = \frac{1}{2\pi} \int_0^\infty dt_1 \int_0^\infty dt_2 e^{i\omega(t_2-t_1)} \langle a(t_1) a^\dagger(t_2) \rangle \propto \int_0^\infty dt_1 \int_0^\infty dt_2 e^{i\omega(t_2-t_1)} \langle P^\dagger(t_1) P(t_2) \rangle \quad (18)$$

Following the approach of [58], we consider the system in a pure state

$$|\psi(t)\rangle = c_g(t)|1, G\rangle + c_e(t)|0, W\rangle \quad (19)$$

and calculate its temporal evolution. The damping of the cavity photons and losses by spontaneous emission are taken into account by using an "effective" non-hermitian Hamiltonian $\tilde{H}_{eff}(t)$ obtained by replacing $\omega_A \rightarrow \omega_A - i\gamma$ and $\omega_c \rightarrow \omega_c - i\kappa$ [31, 32].

In the rotating frame, we can write in the polariton basis :

$$|\tilde{\psi}(t)\rangle = \tilde{c}_+(t)|P_+\rangle + \tilde{c}_-(t)|P_-\rangle \quad (20)$$

with $\tilde{c}_\pm(t) = (\tilde{c}_g(t) \pm \tilde{c}_e(t))/\sqrt{2}$ and $\tilde{H}_{eff}(t)$ is given by

$$\tilde{H}_{eff}(t) = \begin{pmatrix} \omega_0 - \omega_p + \Omega - i\gamma_s & -i\gamma_d \\ -i\gamma_d & \omega_0 - \omega_p - \Omega - i\gamma_s \end{pmatrix} + \frac{\delta\omega_A(t)}{2} \begin{pmatrix} 1 & -1 \\ -1 & 1 \end{pmatrix} \quad (21)$$

with $\gamma_s = \frac{\kappa + \gamma}{2}$ et $\gamma_d = \frac{\kappa - \gamma}{2}$.

We now introduce the two functions $\tilde{b}_+(t)$ and $\tilde{b}_-(t)$ defined by

$$|\tilde{\psi}(t)\rangle = \tilde{b}_+(t) e^{-\gamma_s t} e^{-i(\omega_0 - \omega_p)t} e^{-i\frac{\beta_o}{2} \sin(\omega_m t + \phi)} e^{-i\Omega t} |B_+\rangle + \tilde{b}_-(t) e^{-\gamma_s t} e^{-i(\omega_0 - \omega_p)t} e^{-i\frac{\beta_o}{2} \sin(\omega_m t + \phi)} e^{i\Omega t} |B_-\rangle \quad (22)$$

which are solutions of the two differential equations:

$$\begin{cases} i \frac{\partial}{\partial t} \tilde{b}_+ = - \left(\frac{\beta_o \omega_m}{2} \cos(\omega_m t + \phi) + i\gamma_d \right) e^{2i\Omega t} \tilde{b}_- \\ i \frac{\partial}{\partial t} \tilde{b}_- = - \left(\frac{\beta_o \omega_m}{2} \cos(\omega_m t + \phi) + i\gamma_d \right) e^{-2i\Omega t} \tilde{b}_+ \end{cases} \quad (23)$$

Non-resonant case $\omega_m \ll \Omega$ and small modulation $\beta_o \ll 1$

To calculate the cavity spectrum, we consider first the situation where $\Omega \gg \beta_o \omega_m, \gamma_d$. This is a good approximation of the experiment, which is in a clearly distinct regime than the experiment of Ref. [45]. We can then neglect the fast rotating terms $e^{\pm 2i\Omega t} b_{\pm}$ in the equations 23, which is equivalent to neglect the coupling between the two polaritons. In this case, the solution of the above equations are straightforward:

$$\tilde{b}_{\pm}(t) = \tilde{b}_{\pm}(0) \Rightarrow \tilde{c}_{\pm}(t) = e^{\mp i\Omega t} e^{-\gamma_s t} e^{-i(\omega_0 - \omega_p)t} e^{-i\frac{\beta_o}{2} \sin(\omega_m t + \phi)} e^{i\frac{\beta_o}{2} \sin(\phi)} \tilde{c}_{\pm}(0) \quad (24)$$

Going back to the lab frame, starting from the initial state $|\psi(0)\rangle = |1, G\rangle$, we compute the coefficient of the states $|1, G\rangle$ and $|0, W\rangle$

$$\begin{cases} c_g(t) &= e^{i\frac{\beta_o}{2} \sin(\phi)} e^{-i\omega_0 t} e^{-\gamma_s t} e^{-i\frac{\beta_o}{2} \sin(\omega_m t + \phi)} \cos(\Omega t) \\ c_e(t) &= -ie^{i\frac{\beta_o}{2} \sin(\phi)} e^{-i\omega_0 t} e^{-\gamma_s t} e^{-i\frac{\beta_o}{2} \sin(\omega_m t + \phi)} \sin(\Omega t) \end{cases} \quad (25)$$

We obtain Rabi oscillations at a frequency 2Ω between these two states as in the unmodulated case.

However, the cavity spectrum is modified due to the modulation of the eigenenergies. Noting that $\langle P^\dagger(t_1)P(t_2) \rangle = c_e^*(t_1)c_e(t_2)$, we can indeed write the cavity spectrum as

$$S(\omega) \propto \int_0^\infty dt_1 \int_0^\infty dt_2 e^{i\omega(t_2 - t_1)} c_e^*(t_1) c_e(t_2) \propto \int_0^\infty dt_1 c_e^*(t_1) e^{-i\omega t_1} \int_0^\infty dt_2 c_e(t_2) e^{i\omega t_2} \quad (26)$$

The integrals can be expanded using $e^{-i\beta \sin(\omega_m t + \phi)} = \sum_{n=-\infty}^{+\infty} J_n(\beta) e^{-in\omega_m t} e^{-in\phi}$ and after integration, the cavity spectrum is given by:

$$S(\omega) \propto \left| \sum_{n=-\infty}^{+\infty} J_n(\beta_o/2) e^{-in\phi} \left(\frac{1}{\omega - \omega_0 - n\omega_m + \Omega + i\gamma_s} - \frac{1}{\omega - \omega_0 - n\omega_m - \Omega + i\gamma_s} \right) \right|^2. \quad (27)$$

We see on this expression that multiple frequencies are present in the spectrum, given by $\omega = \pm\Omega + n\omega_m$ with n integer. The peaks of the doublet centered on $\pm\Omega$ acquires multiple sidebands spaced by the modulation frequency ω_m .

Near-resonant case $\omega_m \simeq 2\Omega$

An interesting case occurs when the modulation frequency is close to twice the collective coupling $\omega_m \simeq 2\Omega$ with $\Omega \gg \gamma_d$. In the equations 23, we can then only keep the slowly varying term (rotating wave approximation) and obtain :

$$\begin{cases} i \frac{\partial}{\partial t} \tilde{b}_+ &= -\frac{\beta_o \omega_m}{4} e^{i((2\Omega - \omega_m)t - \phi)} \tilde{b}_- \\ i \frac{\partial}{\partial t} \tilde{b}_- &= -\frac{\beta_o \omega_m}{4} e^{-i((2\Omega - \omega_m)t - \phi)} \tilde{b}_+. \end{cases} \quad (28)$$

After integration, we obtain the population of the polaritonic states (starting from the initial state $|\psi(0)\rangle = |1, G\rangle$):

$$\begin{cases} |c_+(t)|^2 &= \frac{1}{2} (1 - \sin(\phi) \sin(\beta_o \omega_m t / 2)) e^{-2\gamma_s t} \\ |c_-(t)|^2 &= \frac{1}{2} (1 + \sin(\phi) \sin(\beta_o \omega_m t / 2)) e^{-2\gamma_s t}. \end{cases} \quad (29)$$

We clearly see in these expressions that a very effective polaritonic populations transfert occurs at the frequency $\Omega_m = \beta_o \omega_m / 2$ induced by the modulation of the atomic frequency (see Fig. S1). This provides a way to manipulate

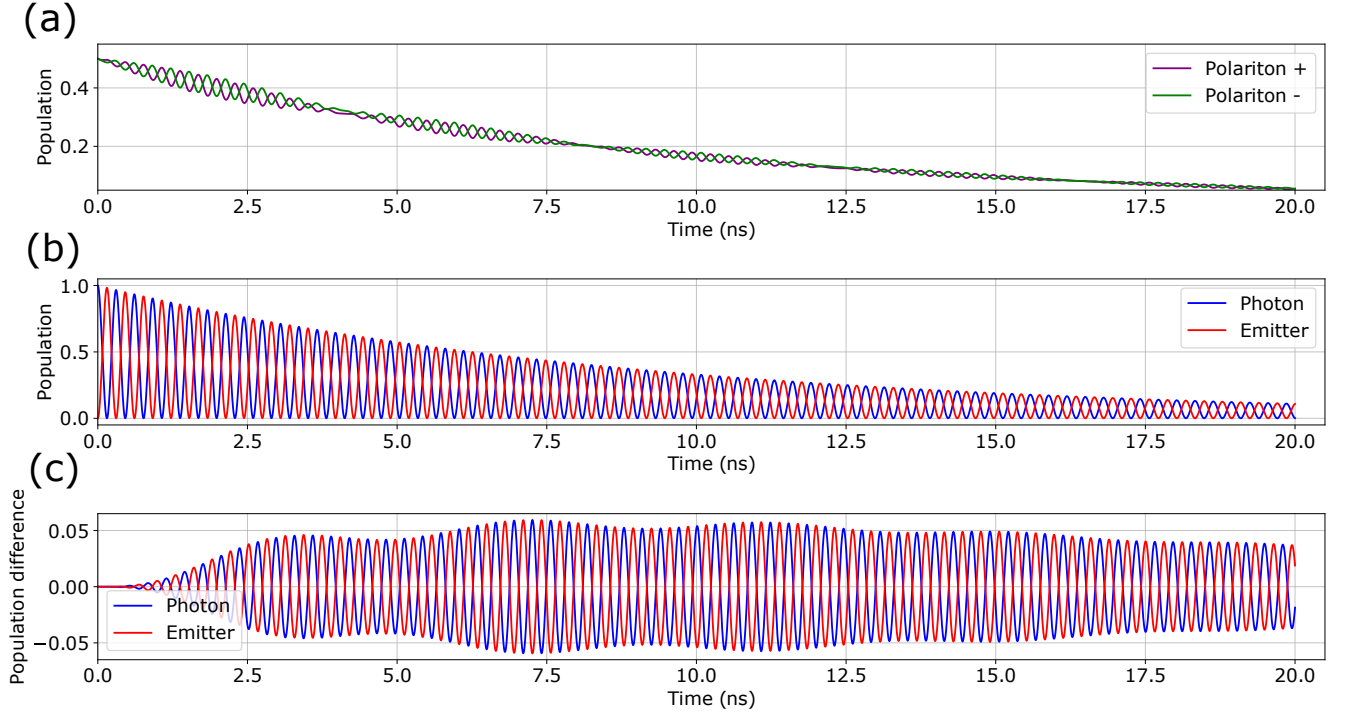


FIG. S1. **Simulation results in the case of a resonant modulation :** $\omega_m = 2\Omega$. The parameters are $\Omega/2\pi = 1634$ MHz, $\kappa/2\pi = 14.6$ MHz, $\gamma/2\pi = 3$ MHz, $\beta_o = 0.17$, $\phi = \pi/2$. (a) Populations of the polaritonic states $|B_+\rangle$ $|B_-\rangle$ defined in the steady state case. The modulation induces a coupling between the two polaritons leading to oscillations at the frequency $\beta_o\omega_m/2$. (b) Modulated Rabi oscillations of the populations of $|1, G\rangle$ and $|0, W\rangle$ (c) Populations difference between the modulated and unmodulated case. (d) Cavity Spectrum for a resonant modulation $\omega_m = 2\Omega$, $\Omega/2\pi = 1634$ MHz, $\kappa/2\pi = 14.6$ MHz, $\gamma/2\pi = 3$ MHz, $\beta_o = 0.17$, $\phi = \pi/2$.

the polaritons on very fast time scales. We note also that the oscillations depend on the phase of the modulation and are maximal for $\phi = \pi/2$ [58].

The expressions of the coefficient $c_g(t)$ and $c_e(t)$ for a phase $\phi = \pi/2$ are given by:

$$\begin{cases} |c_g(t)|^2 = (\cos^2(\Omega_m t/2) \cos^2(\Omega t) + \sin^2(\Omega_m t/2) \sin^2(\Omega t)) e^{-2\gamma_s t} \\ |c_e(t)|^2 = (\sin^2(\Omega_m t/2) \cos^2(\Omega t) + \cos^2(\Omega_m t/2) \sin^2(\Omega t)) e^{-2\gamma_s t}. \end{cases} \quad (30)$$

The populations of these two states feature an oscillation at the frequency 2Ω with a modulation at the frequency $\Omega_m = \beta_o\omega_m/2$ and a damping at rate $2\gamma_s = \kappa + \gamma$ (see Fig.S1).

We calculate the spectrum in this regime, which gives for a resonant modulation $\omega_m = 2\Omega$:

$$S(\omega) \propto \left| \sum_{n=-\infty}^{+\infty} J_n(\beta_o/2) e^{-in\phi} \left(\frac{1 - e^{-i\phi}}{\omega - \omega_0 - 2n\Omega + \Omega(1 + \beta_o) + i\gamma_s} + \frac{1 + e^{-i\phi}}{\omega - \omega_0 - 2n\Omega + \Omega(1 - \beta_o) + i\gamma_s} \right. \right. \quad (31)$$

$$\left. \left. - \frac{1 + e^{i\phi}}{\omega - \omega_0 - 2n\Omega - \Omega(1 + \beta_o) + i\gamma_s} - \frac{1 - e^{i\phi}}{\omega - \omega_0 - 2n\Omega - \Omega(1 - \beta_o) + i\gamma_s} \right) \right|^2.$$

For small modulation depth, the spectrum is dominated by four frequencies $\Omega(1 \pm \beta_o)$ and $-\Omega(1 \pm \beta_o)$, this is the situation depicted on Fig.Fig.S1.d. The different height of the peaks results from the interference between the sidebands of the different terms contributing to the spectrum.

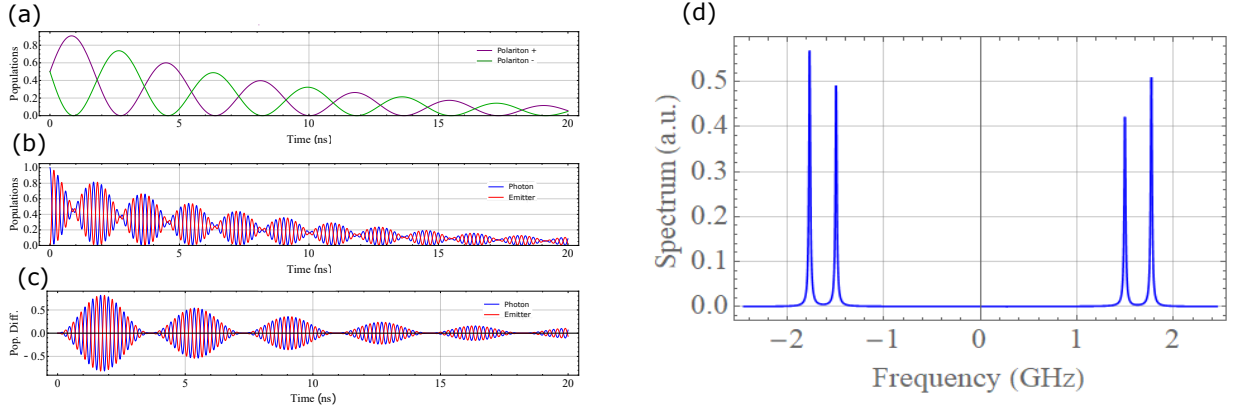


FIG. S2. **Simulation for our experimental parameters:** $\omega_m = 122$ MHz, $g/2\pi = 1634$ MHz, $\kappa/2\pi = 14.6$ MHz, $\gamma/2\pi = 3$ MHz, $\beta_o = 2.17$, $\phi = \pi/2$. (a) Populations of the polaritonic states $|B_+\rangle$ $|B_-\rangle$ defined in the steady state case. The modulation induces a coupling between the two polaritons leading to oscillations at the frequency $\beta_o\omega_m/2$. (b) Modulated Rabi oscillations of the populations of $|1, G\rangle$ and $|0, W\rangle$ (c) Populations difference between the modulated and unmodulated case.

Non-resonant case $\omega_m < 2\Omega$ with non-negligible modulation $\beta_o \geq 1$

In this regime, which corresponds to our experiment, we cannot completely neglect the coupling between the polaritons, so it is not legitimate to perform the rotating wave approximation as it has been done previously. We have integrated numerically the master equation for an initial state with one photon stored in the cavity mode (see Fig. S2). We first see that oscillations occur between the two polaritons at a frequency of about 2Ω . The amplitude of these oscillations is rather small (roughly 4%) due to the fact that the modulation frequency is far-detuned from resonance. A modulation of these oscillations at a frequency $2\omega_m$ is also present, stemming from the anti-resonant term. We can see also Rabi oscillations between the states $|1, G\rangle$ and $|0, W\rangle$ with a slight modulation at the frequency $2\omega_m/2\pi$, clearly visible on the population difference between the modulated and unmodulated case.

Fitting function for experimental spectra

For our experimental parameters, the coupling between the polaritons is relatively weak, so we derive an analytical formula to be able to fit experimental data efficiently. We start from the expression 27 of the cavity spectrum. It can be developed as

$$S(\omega) \propto \sum_n \sum_l J_n(\beta_o/2) J_l(\beta_o/2) e^{-i(n-l)\phi} \left(\frac{1}{(\omega - \omega_0 - n\omega_m + \Omega) + i\gamma_s} - \frac{1}{(\omega - \omega_0 - n\omega_m - \Omega) + i\gamma_s} \right) \times \left(\frac{1}{(\omega - \omega_0 - l\omega_m + \Omega) - i\gamma_s} - \frac{1}{(\omega - \omega_0 - l\omega_m - \Omega) - i\gamma_s} \right) \quad (32)$$

In the experiment, we do not directly measure the cavity spectrum obtained as a Fourier-transform of the temporal oscillation of an initial single excitation. We rather observe the cavity transmission of a weak laser probe swept in frequency, so the phase ϕ is not fixed, and in the equation (23), only the diagonal terms will contribute:

$$S(\omega) \propto \sum_n J_n^2(\beta_o/2) \left| \frac{1}{(\omega - \omega_0 - n\omega_m + \Omega) + i\gamma_s} - \frac{1}{(\omega - \omega_0 - n\omega_m - \Omega) + i\gamma_s} \right|^2 \quad (33)$$

As we are in the regime where $\Omega \gg \omega_m$, we can neglect the crossing terms in the last expression, and we end up with:

$$S(\omega) \propto \sum_n \frac{J_n^2(\beta_o/2)}{(\omega - \omega_0 - n\omega_m + \Omega)^2 + \gamma_s^2} + \sum_n \frac{J_n^2(\beta_o/2)}{(\omega - \omega_0 - n\omega_m - \Omega)^2 + \gamma_s^2} \quad (34)$$